Real-time differential refractometry without interferometry at a sensitivity level of 10^{-6}

Michael McClimans, Charles LaPlante, David Bonner, and Samir Bali

We present a refractometer based on the principle of total internal reflection that can sensitively record, in real time, the refractive index of fluids over a wide range of refractive indices. The device uses a divergent laser beam and a linear diode array, and has no mechanical or optical moving parts, enabling us to achieve the measurement of a refractive index at a sensitivity level of 10^{-6}. Our refractometer does not rely on interferometry, thus enabling the device to be compact, portable, and inexpensive. To the best of our knowledge, this is the first time a noninterferometric device that performs real-time differential refractometry with a sensitivity of better than 10^{-5} has been demonstrated in the literature. We show that our experimental results agree very well with Fresnel theory. We establish a theoretical limit on the sensitivity of this class of refractometers.

OCIS codes: 260.6970, 290.3030, 120.4640, 120.5700, 120.5710, 170.3890.

1. Background and Motivation

Differential refractometry refers to the measurement of small changes in the refractive index of liquids and gases. Such measurement has found increasing use in recent years, with diverse applications ranging from imaging in biological cells[1] and tissues[2–5] and detection of cancerous precursors,[6] to thin-film characterization for the semiconductor industry,[7] chromatography,[8] and even regulation of the fermentation process in the wine industry. For many environmental remediation applications such as the monitoring of pollutants in groundwater, or toxins in air, the real-time measurement of changes in the refractive index with a sensitivity of 10^{-5} or better is desirable, and even necessary.[9] Differential refractometry with a sensitivity of 10^{-5} and better traditionally has been achieved using refractometers based on interferometry.[6,9,10] However, such refractometers are generally not as portable and compact as noninterferometric refractometers and not as amenable to fully automated operation. Noninterferometric refractometers are typically limited to a 10^{-4} sensitivity level,[11,12] with a sensitivity of 10^{-5} being only barely achieved by some expensive, state-of-the-art, commercial refractometers.[13–15] Furthermore, we note that the most commonly used type of refractometer, namely, the Abbe refractometer,[13] is designed for steady-state measurements of isotropic samples and is incapable of recording real-time changes in the refractive index.

We demonstrate a simple optical device that records real-time changes in the refractive index of fluids with a sensitivity of better than 3×10^{-6}. The device design relies on the principle of total internal reflection and is not based on interferometry. Our refractometer consists of no moving mechanical parts, not even a moving optical beam, and is rugged, inexpensive, user friendly, and compact. Specifically, the design is based on the detection of the angular distribution of the intensity of a divergent laser beam that is reflected from the sample onto a linear diode array. Thus the center of each pixel corresponds to a unique angle of incidence on the sample surface. This design is currently used in some new commercially available refractometer models,[14,15] but the resolution of these commercial refractometers is limited to 2×10^{-5} or less. Moreover, the theoretical limit on the sensitivity of this type of refractometer has never been previously explored in the literature. Here we show that the fundamental limit on the sensitivity of this refractometer is not determined by the pitch of the diode array as one may initially suspect, but by the smallest intensity change that can be measured by an individual pixel in the array. We derive a theoretical

The authors are with the Department of Physics, Miami University, Oxford, Ohio 45056-1866. S. Bali's e-mail address is balis@muohio.edu.

Received 23 June 2005; revised 27 December 2005; accepted 24 March 2006; posted 27 March 2006 (Doc. ID 62821).

0003-6935/06/256477-10$15.00/0

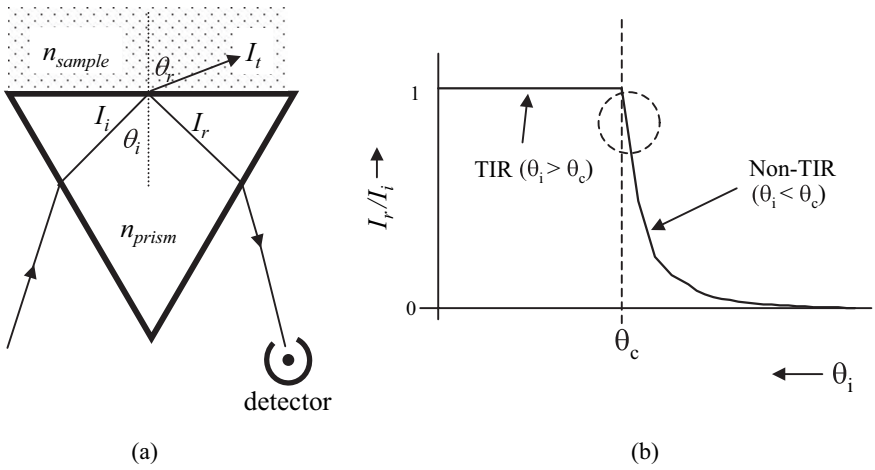

Fig. 1. Principle of TIR-based refractometry. (a) A sample, whose refractive index n_{sample} is to be determined, is placed on the top of the glass prism (refractive index n_{prism}). (b) Representative plot of I_r/I_i versus θ_i, based on Fresnel theory [Eq. (2)]. The regions of TIR and refraction (non-TIR) are indicated. The critical angle θ_c corresponds to the sharp TIR–non-TIR transition. The encircled region is where a small change in θ_i leads to a large change in I_r/I_i. Note that θ_i increases to the left in this figure.

expression for this fundamental limit in terms of the pixel size and dark current, and various other design parameters. We find that, in principle, the sensitivity of this class of refractometers can be better than 10^{-8}, comparable with the best interferometric refractometers.[9,10] In practice, though, the sensitivity is expected to be limited by the intensity fluctuations in the laser to approximately 10^{-7}. Furthermore, we identify other sources of optical noise that may significantly degrade the performance of the refractometer, and we describe methods to suppress their contributions. In this way, by a detailed experimental and theoretical analysis of the different sources of mechanical, electrical, and optical noise, we have been able to demonstrate noninterferometric refractometry at a sensitivity level of better than 3×10^{-6}, i.e., 1–2 orders of magnitude more sensitive than the commercial models mentioned earlier in this paragraph.[14] The demonstrated sensitivity is an order of magnitude less than the expected sensitivity of 10^{-7}, due to our inability to produce, in a controlled manner, samples with closer-lying values of the refractive index. To the best of our knowledge, this is the first time a noninterferometric device that performs real-time refractometry with a sensitivity of better than 10^{-5} has been demonstrated in the literature.

In Section 2 we describe the principle of application of the total internal reflection (TIR) to refractometry. In Section 3 we describe the design and construction of our device and the advantages over previous TIR-based refractometers. In Section 3 we also derive a theoretical expression for the fundamental limit on the device sensitivity owing to pixel dark current and laser intensity fluctuations. Further, we indicate how we suppress noise from other sources, for example, from stray laser light scattered into the pixels. Section 4 describes the calibration of the device. Next, in Section 5, we demonstrate the sensitivity of our refractometer to changes in the sample's refractive index at a few parts in 10^{-6}. Finally, we state our conclusions and future outlook in Section 6.

2. Device Principle: Application of Total Internal Reflection to Refractometry

Consider a glass prism of refractive index n_{prism}, as shown in Fig. 1(a), with a sample of unknown refractive index n_{sample} placed on the top, where $n_{\text{sample}} < n_{\text{prism}}$. Suppose a laser beam of intensity I_i is incident on the prism–sample interface with an angle of incidence θ_i. TIR occurs if θ_i exceeds the critical angle θ_c given by

$$\theta_c = \sin^{-1}(n_{\text{sample}}/n_{\text{prism}}) \tag{1}$$

for the prism–sample interface. In this case one simply obtains unity for the ratio of the reflected intensity I_r to the incident intensity I_i. If $\theta_i < \theta_c$, a transmitted beam I_t refracts into the sample, causing the reflection coefficient I_r/I_i to sharply decrease from unity in accordance with the well-known Fresnel equations of reflection and refraction.[16] For an incident beam that is polarized parallel to the plane of incidence, as is the case for our device, we have by Fresnel theory that[16]

$$\frac{I_r}{I_i} = \frac{\tan^2(\theta_i - \theta_r)}{\tan^2(\theta_i + \theta_r)}, \tag{2}$$

where by Snell's law we have $\sin\theta_r = (n_{\text{prism}}/n_{\text{sample}})\sin\theta_i$. A representative plot of the ratio I_r/I_i as a function of θ_i is shown in Fig. 1(b). The point of sudden departure from unity marks the sharp boundary between TIR and refraction and occurs when $\theta_i = \theta_c$. Thus a careful determination of the location of this boundary enables, in principle, a sensitive measurement of θ_c for the sample, and hence from Eq. (1) the value of n_{sample}. In practice, however, as described in Section 3, the exact location of the critical angle for the I_r/I_i curve is obscured by technical noise (mechanical and/or electrical and/or optical in origin). This prevents discrimination between close-lying values of n_{sample}. In this context, we draw attention to the en-

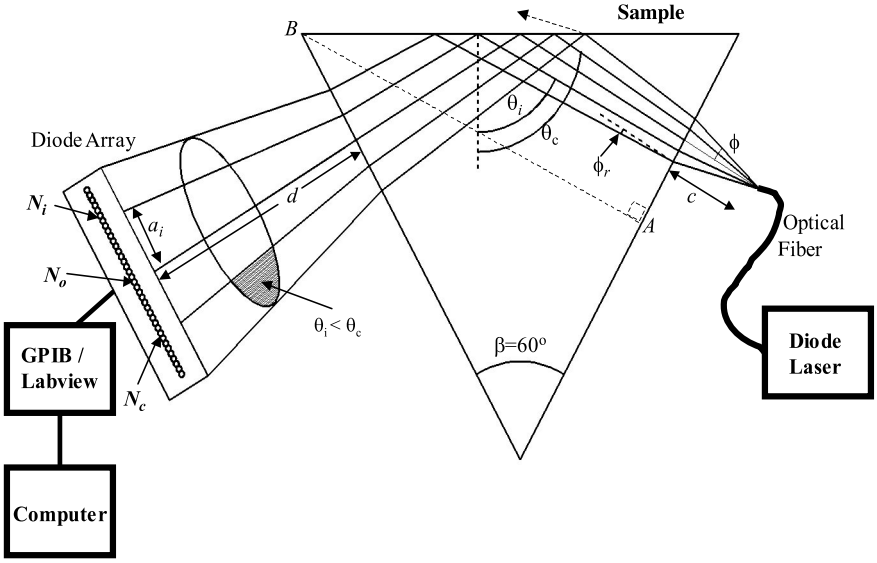

Fig. 2. Schematic of the refractometer. The dashed arrow inside the sample is the refracted ray corresponding to the case of $\theta_i < \theta_c$, which leads to a darkened portion in the beam spot falling on the pixel array. TIR occurs for angles of $\theta_i > \theta_c$. See the text for an explanation of the symbols in the figure.

circled region shown in Fig. 1(b), where θ_i is slightly less than θ_c. In this region we see that for a small change in θ_i there is a large change in I_r/I_i, much larger than any changes that may be caused by noise. In other words, to achieve a relatively noise-free discrimination between close-lying values of n_{sample}, one may examine the region $\theta_i < \theta_c$ in the immediate neighborhood of θ_c rather than just detect the one point $\theta_i = \theta_c$. In Section 4 we shall use this method to sidestep technical noise ripples at the critical angle.

3. Device Design and Construction: Advantages over Existing TIR-Based Refractometers

A. Suppression of Mechanical Noise

The sensitivity of most critical angle-based refractometers[4,5,13] is ultimately limited by the signal-to-noise ratio with which one detects the exact point where the transition from TIR to non-TIR occurs. The most common of these devices is the Abbe refractometer,[13] in which the sample is placed between adjacent prisms and the intensity of the refracted beam passing through the sample from the first prism to the second is measured. Alternatively, the intensity of the reflected ray from the interface of a prism[4] or lens[5] with the sample is monitored as θ_i is varied by rotating a turntable on which the prism or lens is placed. This need for mechanical adjustment of the incident angle to satisfy the requirement $\theta_i = \theta_c$ introduces mechanical noise (which limits device sensitivity), and time delays (which preclude the possibility of real-time refractometry), and often necessitates the presence of an operator (which obviates the possibilities for remote control).

By contrast, in our device all mechanical sources of noise have been practically eliminated. Specifically, in our design, we incorporate the following two components: (1) a *divergent* laser beam instead of a collimated beam, thereby automatically enabling access to many different incident angles simultaneously, and (2) a *linear diode array* to provide position-resolved detection of the angular distribution of light reflected from the sample.

A schematic of our refractometer is shown in Fig. 2. An infrared laser diode (785 nm) is pigtailed to a single-mode optical fiber of mode field diameter 5.8 μm. The numerical aperture of the fiber is 0.12, meaning the divergent Gaussian TEM_{00} beam emerging from the fiber has a half-angle of $\phi = 6.89°$. This beam is incident on an equilateral F2-glass prism (we calculate $n_{\text{prism}} = 1.608925$ for the F2 glass at 785 nm using a dispersion formula supplied by Schott-Optical Glass Technologies) of side = 2.5 cm, such that the center ray of the divergent beam strikes the first prism face at normal incidence. This is accomplished by aligning the retroreflection from the entrance face of the prism back upon the fiber. The angle θ_i represents the angle of incidence of an arbitrary ray within the diverging beam at the prism–sample interface. The fluid sample whose refractive index n_{sample} is to be determined is placed on top of the prism, so that the prism base forms the prism–sample interface. The reflected rays at the prism–sample interface exit from the prism and are allowed to fall on a diode array (Hamamatsu S3903-512Q), driven by a C7884 Hamamatsu circuit driver, which is controlled by LabVIEW through a general-purpose interface bus. The array has a total of 512 pixels. Each pixel has a diameter of 25 μm. Thus the center of each pixel may be associated with a unique incident angle θ_i. Note that in our device there is no moving mechanical component, not even a moving light ray, to keep track. Data taking merely consists of recording the intensity registered by each pixel on the diode array. Thus all mechanical noise is practically eliminated.

B. Fundamental Limit on Refractometer Sensitivity Owing to Pixel Dark Current and Laser Intensity Fluctuations

In the absence of mechanical noise, the sensitivity of our refractometer is limited by electrical and optical

noise arising from the dark current in each pixel and from intensity fluctuations in the laser, respectively.

Figure 2 shows that when the critical angle θ_c for the prism–sample interface lies in the range of angles subtended by the divergent beam, a clear demarcation appears in the reflected beam spot between a lighted portion corresponding to TIR ($\theta_i > \theta_c$) and a dark portion corresponding to non-TIR ($\theta_i < \theta_c$). This "dark edge" marks the location on the pixel array of the critical angle, which moves across the array as the sample's refractive index changes. At first glance it may seem that a given pixel is either bright or dark, meaning that the pitch of the diode array (i.e., the pixel diameter, which is 25 μm in our case) determines the spatial resolution for the location of the dark edge. However, this is not true, for a variation in the location of the dark edge *within a single pixel* leads to measurable changes in the intensity recorded by this pixel. Therefore the resolution of the refractometer is not limited by the pixel diameter but by the smallest intensity change discernible by this pixel; this change, in turn, is clearly limited by the pixel dark current and laser intensity fluctuations.

We first find the geometric relation between the pixel-center position and the incident angle θ_i at the prism–sample interface. The central ray of the divergent beam is perpendicular to the entrance face of the prism, and hence also to the emergent face, because the prism is equilateral. By purely geometric considerations, we find that

$$\theta_i = \beta + \delta_1 + \tan^{-1}\left[a_i\left(b + n_{\text{prism}}(c+d)\frac{\cos\phi_r}{\cos\phi} + \delta_2\right)^{-1}\right], \quad (3)$$

where β is the angle of the prism and is 60° in our case, a_i is the lateral displacement in the detector plane of an arbitrary ray (with incident angle θ_i) from the central ray (see Fig. 2) and can be expressed in terms of the pixel number N_i [see Eq. (4)], b is the total path length of the central ray inside the glass prism (which one may readily verify from geometric considerations to be equal to the dashed line AB drawn in the figure perpendicular to the input face of the prism; $b = 21.7$ mm in our case), c and d are the total path lengths in air of the central ray from the source to the prism and from the prism to the detector plane, respectively ($c = 11$ mm and $d = 20.5$ mm for our particular device), and ϕ_r is the angle of refraction of the boundary ray of the divergent beam cone at the air–prism interface (calculated from Snell's law to be 4.276017° in our case) as shown. In Section 4 the calibration procedure helps determine the symbols δ_1 and δ_2, where δ_1 is the error in degrees denoting the departure from the perpendicular alignment of the central ray onto the entrance face of the prism, and δ_2 is the error in the measurement of the total path length of the central ray from the source to the detector. If we denote as N_i the pixel on whose center the emergent ray corresponding to angle θ_i is incident, and N_0 as the pixel on whose center the central ray is incident, then we also have the following simple relation between a_i and N_i:

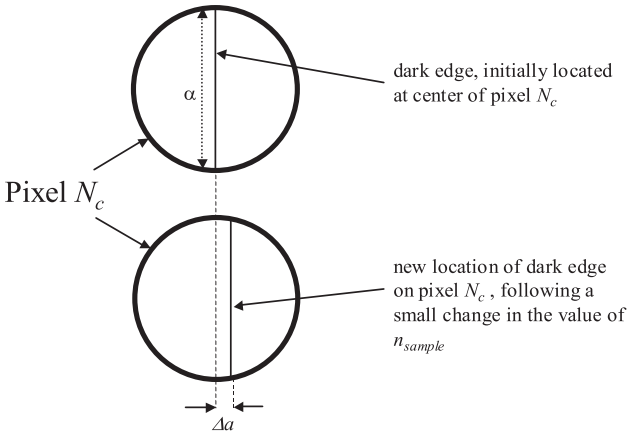

Fig. 3. Calculating the least intensity change discernible by a pixel. The dark edge demarcating the TIR and non-TIR regions moves to a different location within the pixel N_c when the sample's refractive index n_{sample} changes slightly. Assuming the dark edge to be initially located at the center of N_c, the change in illuminated area is $\approx\alpha\Delta a$, where α is the pixel diameter and Δa is the spatial shift of the dark edge.

$$a_i = \frac{N\alpha}{2}\left(\frac{N_0 - N_i}{N_0}\right), \quad (4)$$

where N is the total number ($N = 512$) of pixels in the diode array, and α is the pixel diameter (25 μm), meaning that $N\alpha/2$ is simply equal to half the length of the diode array.

To estimate the least intensity change discernible by a pixel, we assume for convenience that the dark edge corresponding to the critical angle θ_c initially lies at the center of a pixel, which we denote by N_c (see Figs. 2 and 3). Suppose the refractive index of the sample now changes by a small amount, leading to a slight displacement Δa of the dark edge away from the center of this pixel, as shown in Fig. 3. The corresponding change in power ΔP detected by this pixel is given by $\Delta P \approx I\alpha\Delta a$, where I is the total internal reflected laser intensity (≈ 5.1 mW/cm^2 in our case) and $\alpha\Delta a$ is the approximate change in illuminated area. If the response (in mA/mW) of the pixel is denoted by R, the small change in detected photocurrent Δi due to the displacement Δa of the dark edge is given by

$$\Delta i = (I\alpha\Delta a)R. \quad (5)$$

We find from Eqs. (3) and (5) that the corresponding change in the critical angle is

$$\Delta\theta_c \approx \frac{\Delta i}{I\alpha R}\left(b + n_{\text{prism}}(c+d)\,\frac{\cos\phi_r}{\cos\phi}\right)^{-1}, \quad (6)$$

where we have set $\delta_{1,2} = 0$ for the purpose of this theoretical analysis. Further, we have used the ap-

proximation $\tan(\theta_c - \beta) \approx (\theta_c - \beta)$ in radians, because the maximum possible range for $\theta_c - \beta$ is simply given by the beam divergence $\pm\phi_r$ inside the prism, meaning that $\theta_c - \beta$ is small. The relation between the measured change in critical angle $\Delta\theta_c$ and the change in the sample refractive index, denoted by Δn_{sample}, is straightforwardly derived from Eq. (1) as

$$\Delta n_{\text{sample}} \approx \sqrt{{n_{\text{prism}}}^2 - {n_{\text{sample}}}^2}\,\Delta\theta_c. \tag{7}$$

It is clear from Eqs. (5)–(7) that, if we can estimate the smallest measurable value of Δi, we would be able to calculate the sensitivity for our refractometer. The question then is: What is the smallest detectable change in photocurrent Δi? This smallest value is limited by the pixel dark current and/or the fluctuations in the laser intensity.

Role of pixel dark current: If we assume the optical noise to be negligible for now, a reasonable lower limit for Δi is given by the pixel dark current (denoted as i_D). Setting $\Delta i = i_D$ corresponds to a light measurement with a 1:1 signal-to-noise ratio. For our device, the pixel dark current i_D is specified by the manufacturer to be 0.1 pA or less, and the response R is specified to be 0.15 mA/mW. Substituting these values in Eq. (5) we obtain $\Delta a_{\min}$ to be $\approx$0.5 nm, which is over 4 orders of magnitude smaller than the pixel diameter—a remarkable result (which suggests the potential applicability of this simple device to the detection of subnanometric motion of a light beam). From Eq. (6) we find that $\Delta\theta_{c\,\min}$ is predicted to be $\approx 7 \times 10^{-9}$ rad. Then, from Eq. (7), we find that the theoretical limit imposed by the pixel dark current on the sensitivity of our refractometer to changes about $n_{\text{sample}} = 1.333$ (water), say, is approximately 6×10^{-9}, comparable to the most sensitive interferometric refractometers.[9,10]

Role of laser intensity fluctuations: In many cases, instead of the dark current in pixel N_c, it is the fluctuations (denoted by f) in the laser intensity I that may be the dominant factor limiting the sensitivity of the photocurrent to small changes in the sample's refractive index. The fluctuations in the detected photocurrent Δi caused by these laser intensity fluctuations may be written as $\Delta i = fI(\pi\alpha^2/4)R$. In our case, we have measured f in each pixel to be no more than 0.05% by taking 50 measurements of the laser-beam power on the diode array and examining the variance of the voltage signals recorded by each pixel. Thus using previously mentioned values for I, α, and R, we find that $(\Delta i) \approx (5 \times 10^{-4})(5.1\ \text{mW/cm}^2)(\pi/4)(25 \times 10^{-4}\ \text{cm}^2)(0.15\ \text{mA/mW}) \approx 2 \times 10^{-9}$ mA. Substituting this value for ΔI in Eq. (5), we find that the smallest value of Δa that is detectable by the pixel N_c, with a signal-to-noise ratio of 1:1, is given by $f\pi\alpha/4 \approx 10$ nm, which is over 3 orders of magnitude smaller than the pixel diameter. From Eqs. (6) and (7), we find that the smallest measurable value for $\Delta\theta_c$ is predicted to be $\approx 1.4 \times 10^{-7}$ rad, and the theoretical limit imposed by the laser intensity fluctuations on the sensitivity of our refractometer to changes about $n_{\text{sample}} = 1.333$ (water), say, is approximately 1.2×10^{-7}, a factor of 20 higher than the lower limit imposed by the pixel dark current.

Therefore in our case, the optical noise owing to laser intensity fluctuations dominates over the electrical noise owing to pixel dark current and is responsible for setting a theoretical limit of approximately 10^{-7} on the sensitivity of this class of diode-array-based refractometer.

In Subsection 3.C, we describe how data for the intensity distribution reflected from the prism–sample interface are collected and analyzed.

C. Device Operation and Data Analysis: Further Suppression of Optical Noise

We start by measuring the reflected intensity distribution for air (i.e., with no sample present). In this case, the incident angles θ_i at the prism–sample interface are such that the entire Gaussian beam suffers TIR at the prism–air interface, yielding a reflected intensity profile that reproduces the input Gaussian beam, meaning that for all practical purposes the reflected intensity distribution for air is equal to I_i for the diverging beam. The Gaussian beam is centered upon the diode array so that $N_0 = 255$. Curve A in Fig. 4(a) shows the reflected intensity distribution for air (which we refer to as the I_i curve from now on) measured by the diode array as a function of the pixel number.

Next, we measure the reflected intensity distribution I_r for water and various transparent samples of different refractive indices. The samples used are solutions that consist of different concentrations of dimethyl sulfoxide (DMSO) in water. DMSO and water were chosen for their excellent intermiscible properties. DMSO has a refractive index of 1.4780–1.4790 in the temperature range of 20 °C–25 °C. We used sample volumes of approximately 0.5 ml for this work, which was enough to cover the entire prism base. In principle, one merely needs to cover the laser-beam spot (approximate area 0.14 cm^2) on the prism base, meaning far smaller sample volumes may be used if desired. As an auxiliary check of our device and also as a calibration reference, we use a commercial Abbe refractometer which, however, has a resolution limited to only 5×10^{-4}. The Abbe refractometer is calibrated by the manufacturer to provide refractive index values for $\lambda = 589$ nm.

Figure 4(a) shows I_r curves measured for two DMSO–water solutions, namely, S1 and S2, of concentrations of 50% and 30%, respectively (where the concentration value refers to the percentage by volume of DMSO in water), and for distilled water W. The vertical dotted lines in this figure show the location of the transition from the TIR to the non-TIR regime for S1, S2, and W. To give the reader a feel for the refractive indices of these samples, we state the values of n_{sample} as measured by the auxiliary Abbe refractometer for S1, S2, and distilled water, respectively: 1.4065, 1.3770, and 1.3330. Each reflected in-

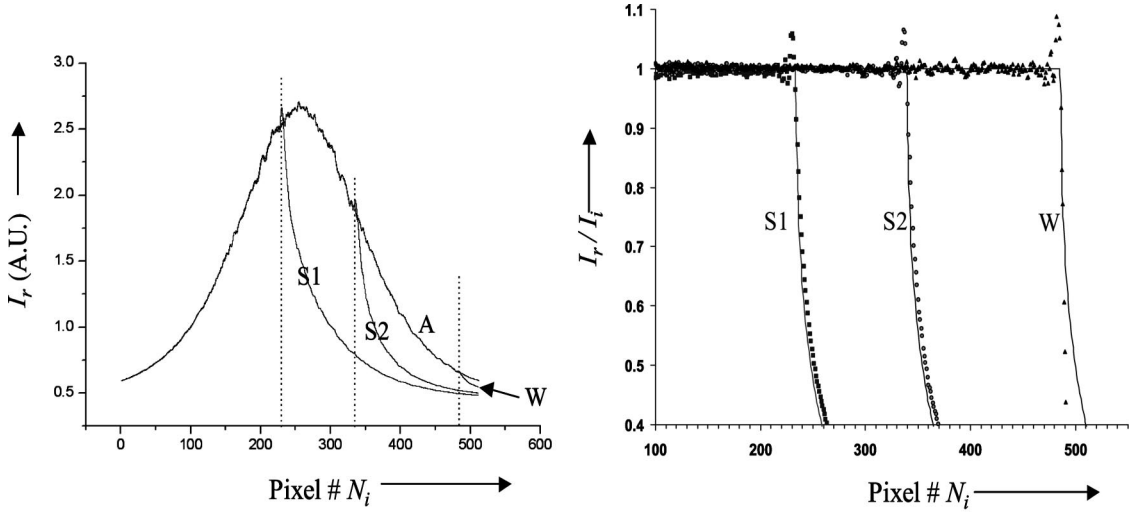

(a) (b)

Fig. 4. (a) Reflected intensity distribution across the diode array for a diverging Gaussian laser beam incident on the prism–sample interface for four different samples: (1) A, "sample" is air. TIR occurs for all incident angles. (2) S1, sample is a 50% DMSO–water solution. (3) S2, sample is a 30% DMSO–water solution. (4) W, sample is distilled water. (b) I_r/I_i curves, corrected for optical noise due to stray laser light scattering as described in the text, for W and samples S1 and S2. The solid curves are theoretical curves obtained from the Fresnel Eq. (2) after device calibration has been performed as described in Section 4.

tensity curve displayed in Fig. 4(a) is an average over 50 scans, and the time taken for each scan is 8.5 ms, implying that our measurements are real time for most practical purposes. The data in Fig. 4(a) have visible contributions from two additional sources of optical noise.

First, the curves in Fig. 4(a) for air A, S1, S2, and water W do not start and end at nearly zero intensity, sitting instead atop an offset of approximately 0.5 V, despite the fact that in our setup the reflected beam spot size at the diode array is less than the length of the array. This is because of the presence of stray scattered laser light from nearby optical components and their mounting hardware. It is important to suppress this noise, otherwise the contribution from noise dominates at small values of I_r. This noise floor is approximately determined for each curve in Fig. 4(a) by finding the minimum I_r value for that curve, which is then subtracted from each measured I_r value to yield a corrected I_r curve. These corrected I_r curves for S1, S2, and W are divided by the corrected I_i curve for air A, and the resultant I_r/I_i curves are plotted in Fig. 4(b), which closely resemble the representative I_r/I_i curve drawn from the Fresnel theory in Fig. 1(b). Superposed on the data in Fig. 4(b) are solid-line curves derived from Fresnel theory, which does not take into account technical noise in any form. An explanation of how these theoretical curves are obtained is provided in Section 4. It is clear from Fig. 4(b) that the agreement between experiment and theory deteriorates only at lower values of reflected intensity, where technical noise due to stray light is expected to dominate, hence the worst agreement for W. But at values of I_r/I_i that are above 0.8 in Fig. 4(b), the agreement between theory and experiment is excellent for all three curves S1, S2, and W.

Second, it is apparent in Fig. 4(a), more so in Fig. 4(b), that noise ripples appear in all the data curves near the TIR–non-TIR boundary, culminating in a large "spike" at the critical angle. We found empirically that the ripple frequency depends on the sample thickness, leading us to speculate that these ripples possibly arise from interference between the front and the back reflections in the sample. At any rate, no matter what the noise source may be, it is vital to circumvent this problem to create a sensitive refractometer. Figure 5 shows a magnified view of the experimental I_r/I_i curves in the critical TIR–non-TIR transition region for three different close-lying DMSO–water solutions, named F1–F3, of concentrations 19.012%, 18.0775%, and 17.2689%, respectively (with refractive index values, as measured with the Abbe refractometer, of 1.3615, 1.3600, and 1.3590, respectively). The solid lines are merely drawn as an aid to the eye. On this magnified scale, the spike looks like a "hump." Clearly, the precise pixel location of the critical transition is ambiguous—does the transition occur at the peak of the hump, or at the beginning or at the end? We decided to alleviate this problem by taking a cue from the comment in Section 2 regarding the encircled region shown in Fig. 1(b), and examining the region *immediately after* the TIR–non-TIR transition in Fig. 5(a), where I_r/I_i falls smoothly from unity in a noise-free manner. In Section 4, we show how we use this noise-free region to calibrate our device for use as a sensitive refractometer.

4. Device Calibration

We calibrate the pixel number N_i in terms of refractive index by the following three steps. First, we choose an I_r/I_i curve (say, F1) in Fig. 5(a), and draw a horizontal

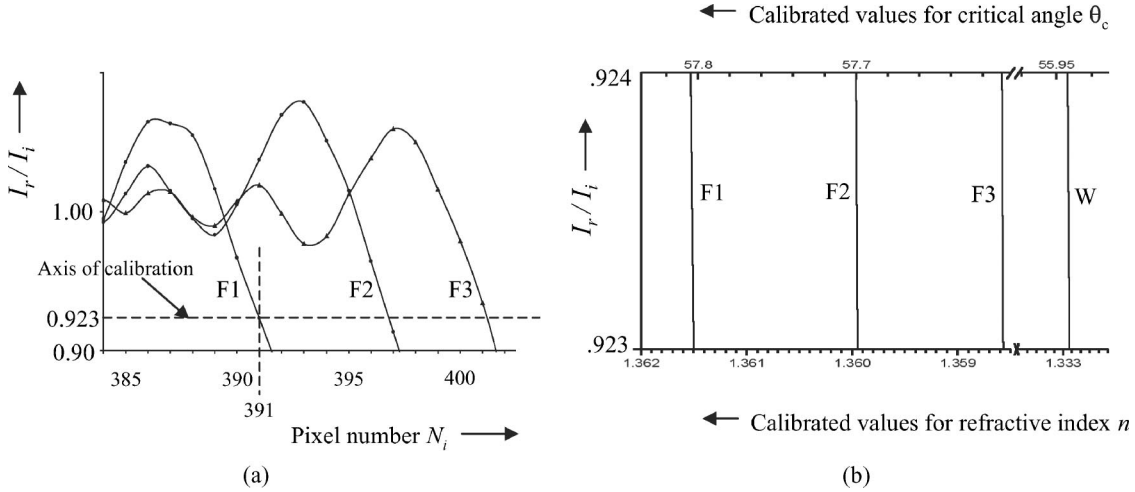

Fig. 5. (a) Magnified view of the I_r/I_i curves in the TIR–non-TIR transition region for three different DMSO–water solutions F1–F3 of close-lying concentrations 19.012%, 18.0775%, and 17.2689%, respectively. The axis of calibration is the horizontal dotted line drawn in the noise-free region near, but not at, the TIR–non-TIR transition point (see Section 4 for further explanation). The reference curve is F1, with all other refractive indices being measured relative to the Abbe value of 1.3615 for F1. The solid lines are merely drawn to aid the eye. (b) Vertically expanded view of the I_r/I_i curves for F1, F2, F3, and distilled water (W) in the vicinity of the axis of calibration which forms the x axis in this figure. Note the break in the x axis to accommodate water in the figure.

dotted line (from now on referred to as the calibration axis) that passes through a pixel data point (say, $N_i = 391$) lying on F1. We postulate that the pixel number at the point of intersection of the calibration axis with the I_r/I_i curve for a given sample corresponds to the critical angle for that sample. Thus $N_i = 391$ is taken to correspond to the critical angle for sample F1. This explains why our refractometer is differential, and not absolute, for it is evident from Fig. 5(b) that the true critical angle would always lie at a smaller (but indeterminate, owing to excessive noise) pixel value. The axis of calibration is chosen to lie close to unity ($I_r/I_i = 0.923$), yet stay well clear of the noise ripples in the data in the TIR region. The exact y location of the axis of calibration is unimportant. Second, we measure the refractive index of the chosen sample F1 with the reference Abbe refractometer ($n_{F1} = 1.3615$ as mentioned earlier) and calculate the critical angle θ_{F1} from this measured value using Eq. (1). Third, we substitute θ_{F1} for θ_i and 391 for N_i in Eq. (3) to obtain an equation in which the misalignment error constants δ_1 and δ_2 are the only two unknowns (the values for all the other symbols were specified in Subsection 3.B). Of the many possible combinations of values that δ_1 and δ_2 may take, yet satisfy Eq. (3), we choose that combination for which both δ_1 and δ_2 are nearly minimized, namely, δ_1 is equal to 0.349111°, and δ_2 is equal to 0.394915 cm. Now, all the parameters on the right-hand side of Eq. (3) are known. Substituting the various pixel numbers into the right-hand side of this equation yields a range of incident angles, each of which transforms into a critical angle for a given sample at the point of intersection of that sample's I_r/I_i curve with the calibration axis. A refractive index may be straightforwardly inferred from each critical angle. Thus the axis of calibration in Fig. 5 is now calibrated in terms of refractive index.

We now check the quality of our calibration by comparing the Abbe measurements for other samples besides F1 [for example, samples F2 and F3 in Fig. 5(a), and water W] with our own device's calibrated measurements of n_{sample}. Figure 5(b) depicts a vertically expanded view near the axis of calibration (which forms the x axis for this figure) of the three I_r/I_i curves F2, F3, and W. The measured refractive indices corresponding to these three curves are read off from their respective points of intersection with the axis of calibration. The comparison between the reference Abbe readings and our calibrated device measurements is shown in Table 1. It is gratifying to note that in each case our refractometer agrees with the Abbe reading to within the resolution of the Abbe refractometer, namely, 5×10^{-4}. In this way, the calibration of our device over the refractive index range of 1.3330–1.3615 is complete. Actually the range of measurable refractive indices extends well beyond 1.3615. A cursory glance at Fig. 4 reveals that, while the TIR–non-TIR transition for water appears near the lower limit of the observable range, we obtained clearly observable critical transitions for refractive indices to approximately 1.43 (the refractive index for sample S1 in Fig. 4 is measured on the Abbe refractometer to be 1.4065). Thus we may achieve the calibration of our device over a rather wide range of refractive indices. Furthermore, in Section 5, we demonstrate that, despite this wide range, our refractometer is sensitive to changes in the refractive index at better than the 10^{-5} level. This is the reason for quoting our refractometer's calibrated readings to the sixth decimal place in Table 1, even though the x axis in Fig. 5(b), which was chosen to display the wide range of calibration, is too coarse to reveal changes on that fine a scale.

Table 1 also shows the theoretical values for n_{sample} predicted by Fresnel theory. To obtain these values,

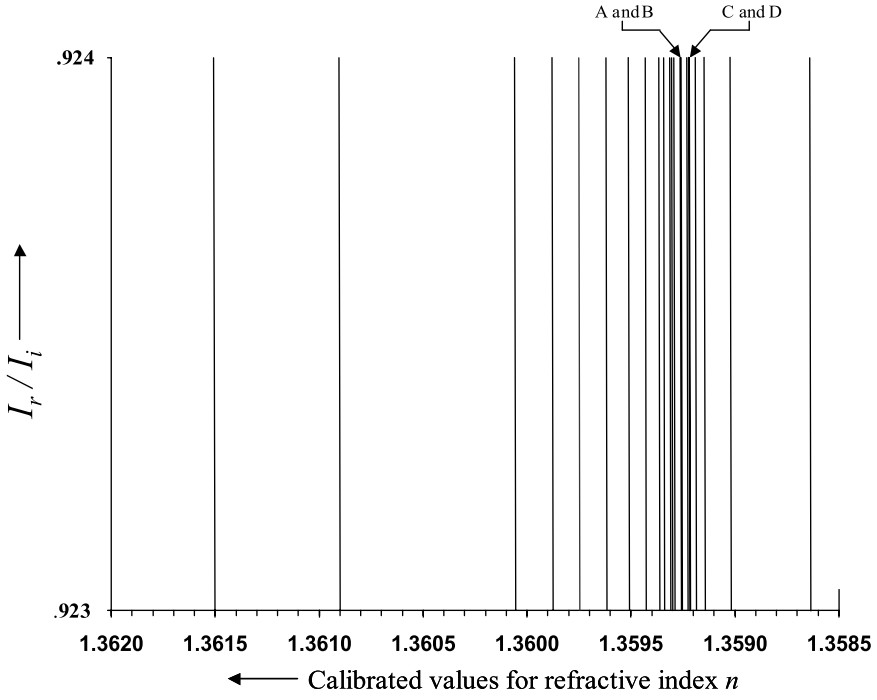

Fig. 6. Twenty-four different DMSO–water samples were systematically prepared so that a wide range of differences in the refractive index may be measured and displayed. All the lines are parallel to each other. Note the "band" formed by the 12 samples with close-lying values of the refractive index. These samples are not distinguished by the Abbe refractometer, but are clearly resolved by our device (see Fig. 7).

we first express Fresnel's formula [Eq. (2)] for I_r/I_i in terms of the pixel number N_i instead of θ_i using the calibration performed just above. Now, for any given sample, we examine Fig. 5(a) and plug into Fresnel's formula the value of N_i at which the sample's I_r/I_i curve intersects with the axis of calibration. We then calculate the value of n_{sample} from Eq. (2) that yields I_r/I_i equal to 0.923 corresponding to our choice of y location of the axis of calibration. For example, for sample F1, we calculate that $n_{\text{sample}} = 1.361556$ at $N_i = 391$ yields 0.923 for I_r/I_i. Note that it is typical for the N_i value at the point of intersection of an I_r/I_i curve with the axis of calibration to be fractional, since a data point will rarely lie at this intersection point. In all such cases, the fractional value of N_i is determined by interpolating between the two pixel data points on the I_r/I_i curve nearest to the calibration axis. We see in Table 1 that the theoretical and experimental values for the refractive indices of F2, F3, and W agree to within the resolution of the reference Abbe. Thus the Fresnel theory offers good support to our experimental results. Once n_{sample} is calculated in this way, the entire theoretical I_r/I_i curve may be generated from Eq. (2). Such theoretical I_r/I_i curves are plotted for samples S1, S2, and water in Fig. 4. Again we find, for S1 and S2, that the theoretical refractive index values of 1.406444 and 1.376977 agree with the Abbe measurements of 1.4065 and 1.3770 within the resolution of the Abbe refractometer.

To conclude this section on device calibration, we note that, instead of using an arbitrary sample as our reference point for calibration, an alternative could be to simply choose the refractive index of water as our reference point. Extensive tables exist in the literature that cite the refractive index of water at different temperatures and wavelengths,[17,18] but in our case we were unsure about the quality of our distilled water, and preferred to do the calibration based on a concrete measurement, albeit with poor resolution. We also note that if we had a high-resolution calibration refractometer, we would use two, not one, reference points for calibration. We would then have two equations for the two unknowns δ_1 and δ_2, meaning we could have then solved for the unknowns exactly, thus enhancing the quality of our calibration.

Table 1. Refractive Indices for Samples F2 and F3 and Water was Measured by Our Abbe Refractometer and Our Calibrated Device[a]

Sample (See Fig. 5; W is in Fig. 4)	Concentration (% by Volume of DMSO in Water)	Refractive Index n_{sample}			Discrepancy ($\times 10^{-4}$)	
		Reference Abbe	Calibrated Device	Theory	Abbe Versus Device	Theory Versus Device
F1	19.0120	1.3615	1.361500	1.361556	0	0.56
F2	18.0775	1.3600	1.359871	1.359908	1.29	0.37
F3	17.2689	1.3590	1.358635	1.358723	3.65	0.88
W (water)	0	1.3330	1.332929	1.332963	0.71	0.34

[a]Both refractometers agree to within the accuracy of the Abbe refractometer.

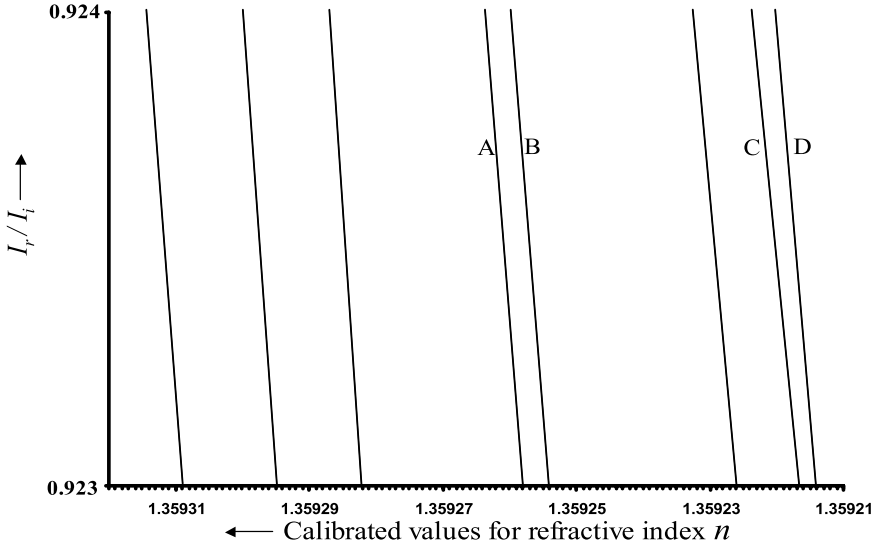

Fig. 7. Eight samples with the closest-lying refractive indices from the curves shown in Fig. 6. The refractive index for an unknown sample is always read from the point of intersection of the I_r/I_i curve for the sample with the calibration axis which is the x axis here. Our device clearly resolves the two pairs of lines A and B, and C and D, for which the differences in the refractive index are 4×10^{-6} and 3×10^{-6}, respectively.

5. Sensitivity of Our Refractometer

We now demonstrate measurements with our refractometer of changes in the refractive index that are significantly smaller than 10^{-5}. Figure 6 shows the I_r/I_i curves for 24 different DMSO–water solutions. These solutions were prepared systematically so that there are several samples for which the refractive indices are not distinguishable on the 10^{-4} scale. For example, none of the 12 samples with a refractive index between 1.3591 and 1.3594 in Fig. 6 was resolvable by the reference Abbe refractometer, least of all the closest-lying samples denoted by A and B, and C and D. Figure 7 demonstrates that our refractometer is capable of clearly distinguishing these close-lying samples. The fact that the lines no longer look vertical is irrelevant because only their points of intersection with the axis of calibration (the x axis in Fig. 7) matter. Note that the least count of the x axis in Fig. 7 is 10^{-6} units of refractive index. Thus samples A and B are demonstrated to be separated in the refractive index by 4×10^{-6}, and samples C and D are separated by less than 3×10^{-6}. The reason we could not probe even smaller refractive index changes was that we had no method for preparing samples in a controlled manner with ever-decreasing differences in the refractive index.

The data in Figs. 4–7 clearly show that our refractometer performs highly sensitive measurements of changes in the refractive index over a wide range of indices. The current data were taken with no temperature stabilization on the device leading to a temperature fluctuation of 0.5 °C over approximately 30 min. As a result, it was difficult to prepare DMSO–water solutions in a controlled fashion for which the refractive index differed by a few parts in a million or less.

6. Conclusions

In conclusion, we have built a proof-of-principle refractometer, which we have demonstrated is sensitive to changes in the refractive index at a level less than 3×10^{-6}. The determination of the refractive index of an unknown sample is completed in less than a second, and is hence near real time. Most biological imaging applications focus on samples for which the refractive index is close to that of water. The refractive index for water lies too close to the end of our useful range in the setup described in this work. However, by simply changing the prism to a lower refractive index (for example, BK7 glass with a refractive index of 1.517), one may center the usable range of refractive indices upon water for bioimaging purposes. Sample sizes need not be larger than a fraction of 0.5 ml. The high quality of the data in Fig. 7, and the theoretical analysis in Subsection 3.B of the fundamental limit on the sensitivity of this class of refractometer, suggests that the device is capable of resolving differences in the refractive index even smaller than 10^{-6}. However, we could not test the sensitivity of the device at that level because of our inability to produce samples with refractive indices lying that close. Temperature stabilization, and increasing the number of pixels from 512 to 1024, are obvious steps to improve the sensitivity of the device. Even so, this is the first time, to the best of our knowledge, that a noninterferometric refractometer capable of real-time measurements with better than 10^{-5} sensitivity has been demonstrated.

From the point of view of bioimaging, the measurement of refractive index of turbid and absorbing samples is of great interest. Our refractometer offers the potential for highly sensitive differential refractometry at the 10^{-4}–10^{-6} level. Traditional critical angle-based refractometers[14,15] fail with such samples, because they examine only the one point $\theta_i = \theta_c$. It is well known that near the critical angle, the beam experiences substantial penetration into the sample before undergoing reflection back out (this is the Goos–Hanchen effect). The scattering during this penetration causes a nonzero imaginary component of the refractive index and has been shown to have a smoothing effect on the sharp knee in the reflectance-

versus-incident angle curve.[19] Furthermore, in this case, the "critical" angle at which the maximum reflectance change occurs has been shown[19] to yield erroneous values for the real part of the refractive index. In our refractometer design we examine not just $\theta_i = \theta_c$ but the nearby region $\theta_i < \theta_c$. As demonstrated in Subsection 3.C and Section 4, one may perform exceptionally sensitive differential refractometry by steering clear of the noisy TIR–non-TIR region and instead working in a nearby noise-free region. Clearly, this is appropriate only if the slope of the I_r/I_i curve *at the calibration axis* [see Fig. 5(a)] is the same for every sample refractive index. We checked that this is indeed the case for the theoretical curves derived from Fresnel theory [see Eq. (2)] that are used to fit all the data presented in Figs. 6 and 7. Note that, once the pixel array is calibrated in terms of refractive index values [see Fig. 5(a)], the slope of the intensity change I_r/I_i is nothing but the sensitivity of the device. In other words, the theoretical sensitivity of the device is constant over the range of sample refractive indices examined in this work.

Further bioapplications of our device may be envisioned if we examine changes in the *polarization* of the totally internally reflected light, caused perhaps by biological activity at different spatial points in the sample.[20] These possible applications are currently being investigated in our laboratory.

We gratefully acknowledge invaluable discussions with L. M. Bali and R. Sah. We also acknowledge the extremely helpful and insightful suggestions made by an anonymous referee, and Lynn Johnson in the Miami University Instrumentation Laboratory. Financial support from the Research Corporation and the Petroleum Research Fund is gratefully acknowledged. An application for a patent has been filed for the refractometer described in this work.

References

1. J. Beuthan, O. Minet, J. Helfmann, M. Herrig, and G. Muller, "The spatial variation of the refractive index in biological cells," Phys. Med. Biol. **41,** 369–382 (1996).
2. F. Bolin, L. Preuss, R. Taylor, and R. Ference, "Refractive index of some mammalian tissues using a fiber optics cladding method," Appl. Opt. **28,** 2297–2303 (1989).
3. J. M. Schmitt and G. Kumar, "Turbulent nature of refractive-index variations in biological tissue," Opt. Lett. **21,** 1310–1312 (1996).
4. J. Lai, Z. Li, C. Wang, and A. He, "Experimental measurement of the refractive index of biological tissues by total internal reflection," Appl. Opt. **44,** 1845–1849 (2005).
5. H. Li and S. Xie, "Measurement method of the refractive index of biotissue by total internal reflection," Appl. Opt. **35,** 1793–1795 (1996).
6. C. Yang, A. Wax, I. Georgakoudi, E. Hanlon, K. Badizadegan, R. R. Dasari, and M. S. Feld, "Interferometric phase-dispersion microscopy," Opt. Lett. **25,** 1526–1528 (2000).
7. T. Kihara and K. Yokomori, "Simultaneous measurement of refractive index and thickness of thin film by polarized reflectances," Appl. Opt. **29,** 5069–5073 (1990).
8. D. J. Bornhop, T. G. Nolan, and N. J. Dovichi, "Subnanoliter laser-based refractive index detector for 0.25-mm I. D. microbore liquid chromatography," J. Chromatogr. **384,** 181–187 (1987).
9. M. L. Eickhoff and J. L. Hall, "Real-time precision refractometry: new approaches," Appl. Opt. **36,** 1223–1234 (1997).
10. R. G. Johnston and W. K. Grace, "Refractive index detector using Zeeman interferometry," Appl. Opt. **29,** 4720–4724 (1990).
11. A. Leung and J. Vandiver, "Automatic refractometer," Opt. Eng. **42,** 1128–1131 (2003).
12. L. M. Bali, R. K. Shukla, P. Srivastava, A. Srivastava, A. Srivastava, and A. Kulshreshtha, "New approach to the measurement of refractive index," Opt. Eng. **44,** 058002–058008 (2005), and references therein.
13. See, for instance, J. Rheims, J. Kosery, and T. Wreidt, "Refractive-index measurements in the near-IR using an Abbe refractometer," Meas. Sci. Technol. **8,** 601–605 (1997), and references therein.
14. K-Patents, Inc., Model PR-03-D, www.kpatents.com, U.S. patent 6,760,098 B2, Harri Salo (July 2004).
15. Topac, Inc., DUR series, www.topac.com.
16. See, for example, M. A. Heald and J. B. Marion, *Classical Electromagnetic Radiation,* 3rd ed. (Saunders College Publishing, 1995).
17. D. Segelstein, "The complex refractive index of water," M.S. thesis (University of Missouri-Kansas City, 1981).
18. R. M. Pope and E. S. Fry, "Absorption spectrum (380–700 nm) of pure water. II. Integrating cavity measurements," Appl. Opt. **36,** 8710–8723 (1997).
19. G. H. Meeten and A. N. North, "Refractive index measurement of absorbing and turbid fluids by reflection near the critical angle," Meas. Sci. Technol. **6,** 214–221 (1995).
20. S. Venkatasubbarao, N. Beaudry, Y. Zhao, and R. Chipman, "Evanescent-imaging-ellipsometry-based microarray reader," J. Biomed. Opt. **11,** 014028 (2006).